Tunable metamaterial response of a $Ni_{80}Fe_{20}$ antidot lattice for spin waves

S. Neusser,[1] H. G. Bauer,[2] G. Duerr,[1] R. Huber,[1] S. Mamica,[3] G. Woltersdorf,[2] M. Krawczyk,[3] C. H. Back,[2] and D. Grundler[1,*]

[1]*Lehrstuhl für Physik funktionaler Schichtsysteme, Technische Universität München, Physik Department, James-Franck-Str. 1, D-85747 Garching b. München, Germany*

[2]*Institut für Experimentelle und Angewandte Physik, Universität Regensburg, D-93040 Regensburg, Germany*

[3]*Surface Physics Division, Faculty of Physics, Adam Mickiewicz University, Umultowska 85, PL-Poznań 61-614, Poland*

(Received 5 May 2011; published 14 November 2011)

All-electrical spin-wave spectroscopy and frequency-resolved magneto-optical Kerr-effect measurements are combined to study spin waves propagating through a magnetic antidot lattice nanopatterned from a $Ni_{80}Fe_{20}$ thin film. Spin waves are injected from a plain film into the antidot lattice and the transmission across the interface is explored in detail for different wavelengths. We find that spin waves with a wavelength much greater than the lattice periodicity are not described well by recently discussed approaches. Instead the spin-wave dispersion is consistent with an effective magnetization smaller than the saturation magnetization measured on the unstructured ferromagnetic material. Consistently, we find that the transmission coefficients are modeled well by assuming an effectively continuous metamaterial for spin waves characterized by the reduced magnetization. The experimental data and interpretation are substantiated theoretically using the plane-wave method and micromagnetic modeling. The results are interesting for the development of frequency-selective mirrors in magnonics through lateral nanopatterning.

DOI: 10.1103/PhysRevB.84.184411 PACS number(s): 75.40.Gb, 76.50.+g, 75.30.Ds

I. INTRODUCTION

For electromagnetic waves it is known that a periodically patterned material with a unit cell much smaller than the incident wavelength can change the propagation properties; if effective or continuous properties describe the dynamic response of the patterned medium, it is referred to as a metamaterial (MM).[1] In magnetism an effective-medium theory has been developed for superlattices that incorporate magnetically ordered films. The theory has allowed one to replace the superlattice by an effective medium to describe the collective spin excitations in periodically arranged magnetic materials.[2–6] In a superlattice-based nanowire the dependence of the effective magnetic parameters on the individual layer parameters has been shown to differ from the arithmetic average over the volume of the superlattice. This provokes MM characteristics for collective spin excitations.[7] Effective materials properties have also been considered for patterned ferromagnets in a planar configuration.[8,9] Still, effective parameters of periodically nanopatterned ferromagnets as considered in the present article are rarely addressed and, therefore, not yet covered by recent reviews on metamaterials.[10–12] For electromagnetic waves, the transmission *across* the boundary from a conventional material into a periodically patterned MM has attracted considerable attention due to phenomena such as negative refraction, perfect lenses, and electromagnetic cloaks.[13–15] The reflection of electromagnetic radiation from structured metallic magnets has been studied using the effective-medium theory in Ref. 16. The reflection of spin waves (SWs) has been considered at inhomogeneities[17,18] and heterogeneous interfaces between different materials.[19–23] However, the SW propagation across an interface between a conventional ferromagnetic film and an effective medium for spin waves created by nanopatterning has not yet been addressed to the best of our knowledge. Such lateral magnetic MMs would certainly open further perspectives in the research field of magnonics[24,25] where one aims at full control over propagation properties of the spin waves.

In this article we study the propagation of SWs through an array of holes, i.e., an antidot lattice (ADL), with periodicity $p = 800$ nm. The hole diameter of $d = 120$ nm is much smaller than both p and the SW wavelength of a few μm. By the holes, only 1.7% of the magnetic material is removed; however, the dynamic response is altered significantly. We observe novel behavior of propagating SWs within this material and, in an independent experiment, for the transmission of long-wavelength SWs across the interface between a conventional ferromagnetic film and the ADL. Both the SW dispersion and the wavelength-dependent transmission coefficients are found to be consistent with an effectively continuous parameter such as the effective magnetization, M_s^*. The effective magnetization is not just the arithmetic average over the ferromagnetic material and the air holes. The SW localization and SW channeling effects previously reported for short wavelength SW in antidot lattices[26–29] completely fail to explain the data. We substantiate our findings on metamaterial behavior using the plane-wave method and micromagnetic modeling.

This article is organized as follows: First, in Sec. II A, the sample geometry, all-electrical spin-wave spectroscopy (AESWS), and magneto-optical Kerr (MOKE) effect are introduced. In Sec. II B we discuss the theoretical background, including the plane-wave method (PWM). Experimental results are presented in Sec. III. In Sec. III B, the SW dispersion within an ADL is discussed. In Secs. III C and III D the dependence of the transmission coefficient of SWs into the ADL is experimentally studied for different frequencies and orientations of the external field. Finally, in Secs. IV A and IV B, the experimental data are analyzed and interpreted using the theoretical methods of the plane-wave method and micromagnetic simulations. Section V contains the discussion before we conclude in Sec. VI.

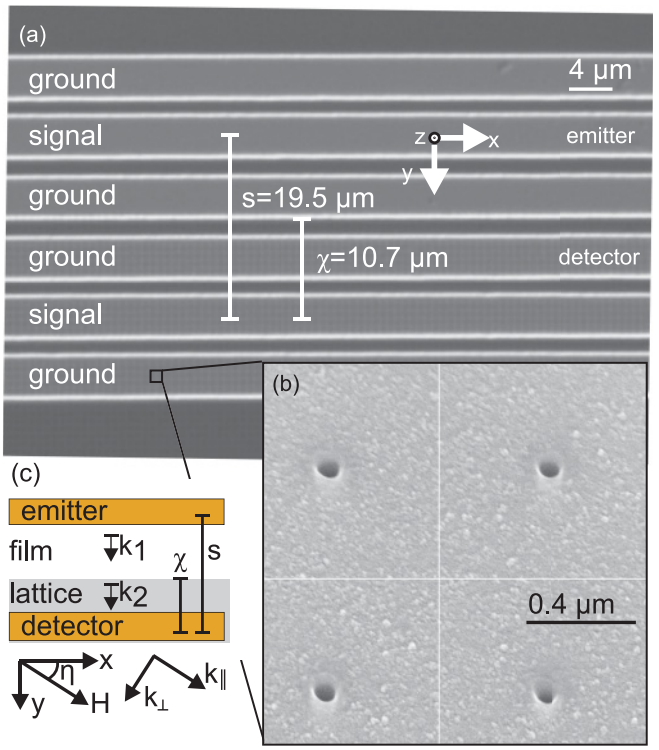

FIG. 1. (Color online) (a) Optical micrograph of sample 3. Two collinear CPWs for AESWS are integrated on top of a hybrid device consisting of a plain film and an ADL. The inner conductors of the CPWs act as emitter and detector of spin waves. The separation in y direction is $s = 19.5$ μm. The additional metal stripes are ground lines. (b) Scanning electron microscopy image showing focused ion-beam-etched holes. The circular holes (diameter of 120 nm) are arranged on a square lattice with a period $p = 800$ nm. (c) Sketch of the AESWS experiment. CPWs labeled emitter and detector are integrated with a sample partially structured into an antidot lattice (gray area) extending along the x axis. SWs are excited in the plain film with a wave vector k_1 pointing in the y direction. Behind the film-ADL boundary SWs are scattered to a wave vector k_2. The orientation of the field with the x axis is given by the angle η.

II. EXPERIMENTAL AND THEORETICAL BACKGROUND

A. Sample layout, AESWS, and MOKE techniques

We have fabricated the ADL into a $Ni_{80}Fe_{20}$ thin film (thickness $t_s = 25$ nm as determined via atomic force microscopy) using focused ion beam etching of a periodic square lattice of holes [Figs. 1(a) and 1(b)]. The period is $p = 800$ nm and hole diameter is $d = 120$ nm. This corresponds to a $Ni_{80}Fe_{20}$ filling fraction of $\mathcal{F} = 1 - \pi(d/2)^2/p^2 = 0.983$, i.e., only 1.7% of the magnetic material is missing. The diameter d is taken as an averaged value over many holes. Due to edge roughness the diameters vary on the 10-nm scale. The squared ADL unit cell is aligned with the x and y axes. Using the magneto-optical Kerr effect we measure the coercive and saturation fields for different orientations of the applied in-plane field $\mathbf{H}$. For the different angles the coercive (saturation) field is found to be below 4.8 mT (9.5 mT). Subsequently, the antidot lattice is capped using SiO_2. To ensure excitation and detection of SWs in the long wavelength limit (LWL), we integrate two coplanar wave guides (CPW) of 4-μm inner conductor width each on top of the SiO_2. They serve as an emitter and detector of SWs. The distance between the centers of the two inner conductors is $s = 19.5$ μm throughout this work. The CPWs are collinear with the x axis such that the transferred wave vector $\mathbf{k}$ is orientated along the y axis [Fig. 1(c)]. In the experiment a GHz current of frequency f is applied to the inner conductor using the output of a vector network analyzer (VNA). The inhomogeneous magnetic field $\mathbf{h}_{rf}$ excites SWs via the torque $\mathbf{M} \times \mathbf{h}_{rf}$, where $\mathbf{M}$ is the magnetization. The relevant wave vectors k_{CPW} of emitted SWs cover the range $\Delta k = 0.2 \ldots 1.5$ rad/μm. The first Brillouin zone (BZ) of the ADL ends at $\pi/p = 3.9$rad/μm, so $k_{CPW}/(\pi/p) \approx 0.05 \ldots 0.4$. This allows us to cover the LWL. In general, the emitted and detected wave vector at a given frequency f might not be equivalent. We label them k_1 and k_2, respectively. SWs are detected connecting the CPW to the detector input of the VNA. In the experiments discussed here we apply a static magnetic field $\mu_0 H = 20$ mT that is larger than both the coercive and saturation fields. At this field, the magnetization $\mathbf{M}$ of the given antidot lattice is almost fully aligned with $\mathbf{H}$. The orientation of $\mathbf{H}$ is varied. The angle η is defined between $\mathbf{H}$ and the x axis [Fig. 1(c)]. The angle between $\mathbf{H}$ and $\mathbf{k}$ is then given by $90^\circ - \eta$. The wave-vector components perpendicular (parallel) to $\mathbf{H}$ are denoted $k_\perp$ ($k_\parallel$) in the following. For $\eta = 0$, $\mathbf{k} \perp \mathbf{H}$, i.e., $k_\perp = |\mathbf{k}|$.

For all-electrical spin-wave spectroscopy (AESWS) using two CPWs it is in particular important to measure separately the excitation and detection efficiency of each CPW. We do this by measuring SW signals at the emitter and detector CPWs in reflection configuration. The signal amplitudes measured by the VNA are denoted by a_{11} and a_{22}, respectively. If the sample is symmetric, then $a_{11} = a_{22} \equiv a_0$. In transmission measurements the SWs are emitted at one CPW, i.e., the SW emitter; they propagate through the ferromagnet and are then detected by the second CPW, the SW detector. The signal amplitude of SWs at the detector is denoted a_{21}. To obtain such signal amplitudes, we always make use of a reference technique. For $\eta = 90^\circ$ and $\mu_0 H = 100$ mT, a reference data set is obtained lacking a SW signal because the torque $\mathbf{M} \times \mathbf{h}_{rf}$ is essentially zero. This reference data set is subtracted from the subsequent spectra to eliminate the nonmagnetic background signal.[30] The reflection and transmission signals are related via[31,32]

$$\frac{a_{21}}{a_0} = \exp\left(-\frac{s}{v_g \tau}\right) = \exp(-s\xi), \qquad (1)$$

where v_g is the SW group velocity, τ is the SW relaxation time, and ξ is the inverse SW decay length. Both transmission (a_{21}) and reflection (a_0) data depend on the orientation of the external field η and the frequency f.

In the following we discuss results obtained on three complementary samples (Table I): sample 1 is formed by a plain

TABLE I. Overview of $Ni_{80}Fe_{20}$ thin-film samples studied by all-electrical spin-wave spectroscopy.

	Sample 1	Sample 2	Sample 3
Type	Plain film	Full ADL	Film/ADL
χ (μm)	0	$>19.5 = s$	10.7

film between emitter and detector CPW. Sample 2 consists of a full antidot lattice (ADL) covering the whole area underneath and between the two collinear CPWs. The width χ of the ADL that is measured along the transverse direction to the CPWs is thus larger than $s = 19.5\ \mu$m. χ denotes the extension of the antidot lattice measured from the center of the detector CPW in the direction toward the emitter CPW. Sample 3 is peculiar in that SWs are excited in a plain film and transmitted across a boundary into an ADL. The boundary is parallel to the CPWs, i.e., perpendicular to **k**. In this hybrid device we pattern the ADL such that SWs travel a distance of $\chi = 10.7\ \mu$m within the ADL before reaching the inner conductor of the detector CPW. The distance χ is thus smaller than the CPW separation s. For all samples we will discuss the signal amplitudes a_{11}, a_{22}, and a_{21}. Note that sample 3 is no longer symmetric with respect to emitter and detector CPWs and $a_{11} \neq a_{22}$. Sample 1 is found to exhibit the largest relaxation time τ as already reported for an unpatterned film.[32] Here we are able to follow the SW propagation signal over a broad frequency range, allowing us to extract the propagation velocity v_g from coherent phase changes as discussed in Refs. 31,32.

To obtain local information on propagating spin waves we apply the spatially resolved MOKE. We make use of the polar Kerr signal. The spatial resolution is about 250 nm. We do not use pulsed excitation of the magnetization in the MOKE data discussed here. Instead, a single-frequency continuous wave (cw) microwave excitation is applied to the integrated CPW and then used to study the SWs formed for different frequencies f.[33–35] For this the scanning MOKE setup is combined with a microwave generator allowing us to probe the microwave-induced spin precession by optical means. The laser probe pulses arrive at a repetition rate of 80 MHz. Locking the cw microwave source to the clock of the laser ensures that the laser probe pulses always arrive at the same phase of the excitation. A mechanical time delay between the source of the excitation and the sample allows us to shift the phase of the excitation with respect to the laser probe pulses. Thus, the response of the magnetic sample can be investigated at any phase of the exciting wave. At the same time the scanning unit of the MOKE setup allows us to position the laser at different lateral distances from the CPW. By this means we acquire phase- and spatially resolved spin precession profiles of the spin waves excited by the microwave field h_{rf} of the CPW. The phase-sensitive scanning MOKE technique is particularly powerful both in measuring the dispersion relations $f(k)$ in the different devices considered here and detecting SWs reflected at the boundary between the thin film and the ADL of sample 3. Considering the same excitation mechanism using a CPW attached to a microwave generator, the modes addressed by the magneto-optical and all-electrical experiments can be directly compared. For MOKE and AESWS the microwave amplitude is chosen such that we stay in the linear regime,[34,36] i.e., at small precession amplitudes consistent with the plane-wave method outlined below.

B. Theoretical background and modeling

When a wave travels across the boundary between two media, in general, transmission and reflection occur at the interface. The transmission coefficient reads[37]

$$t(f) = \frac{2k_2(f)}{k_1(f) + k_2(f)}. \tag{2}$$

Here, k_1 and k_2 at frequency f are assumed to be perpendicular to the interface and the relevant wave vectors of medium 1 and 2, respectively. In a cw experiment the reflected wave in general interferes with the incident wave. This gives rise to a characteristic wave pattern between the emitter and the boundary. In the following, we present the formalism how to treat the interference pattern when a SW transmitted from the emitter in medium 1 (plain film) needs to enter the medium 2 (ADL). A fraction r of the SW amplitude is back-reflected at the boundary and returns into the plain film. In the cw experiment of fixed f, the reflected SW interferes with the incident one. This results in a superposition of two sinusoidal waves,

$$a_{\mathrm{in}}^{\mathrm{film}}(y) = a_{0,\mathrm{in}}^{\mathrm{film}} \exp(-ik_1 y) \exp(i\omega t) \tag{3}$$

and

$$a_{\mathrm{out}}^{\mathrm{film}}(y) = a_{0,\mathrm{out}}^{\mathrm{film}} \exp[ik_1(y - y_0)] \exp(i\omega t), \tag{4}$$

where $a_{0,\mathrm{in}}^{\mathrm{film}}$ describes the incident spin-wave amplitude, $a_{0,\mathrm{out}}^{\mathrm{film}}$ describes the reflected spin-wave amplitude, and y_0 marks the position of the boundary. The reflected and incident amplitudes are connected via

$$a_{0,\mathrm{out}}^{\mathrm{film}} = r\left|a_{\mathrm{in}}^{\mathrm{film}}(y_0)\right|. \tag{5}$$

The total amplitude is given by

$$\begin{aligned} a(y) = \left|a_{\mathrm{in}}^{\mathrm{film}}(y) + a_{\mathrm{out}}^{\mathrm{film}}(y)\right| \approx a_{0,\mathrm{in}}^{\mathrm{film}} \exp(-\xi^{\mathrm{film}} y) \\ + a_{0,\mathrm{out}}^{\mathrm{film}} \exp[\xi^{\mathrm{film}}(y - y_0)] \cos[k_1(2y - y_0) + \delta]. \end{aligned} \tag{6}$$

This is obtained by neglecting terms $\propto r^2$. ξ^{film} is the inverse decay length of the SW in the plain film, i.e., the imaginary part of the wave vector $\xi^{\mathrm{film}} = \mathrm{Im}k_1$. The cosine term describes the interference of both SWs between the CPW and the ADL boundary. We will use the cw microwave excited MOKE experiment to measure the interference pattern along the y direction between the emitter and the boundary.

To analyze our experimental results in detail, we perform calculations based on the PWM and micromagnetic simulations. Details of PWM are described elsewhere.[38] Here we restrict ourselves to a short discussion of the principles. The Landau Lifshitz equation is the equation of motion of the magnetization:

$$\frac{\partial \mathbf{M}(\mathbf{r},t)}{\partial t} = -\gamma\mu_0[\mathbf{M}(\mathbf{r},t) \times \mathbf{H}_{\mathrm{eff}}(\mathbf{r},t)], \tag{7}$$

where γ is the gyromagnetic ratio ($\gamma > 0$), μ_0 is the vacuum permeability, and $\mathbf{H}_{\mathrm{eff}}$ is the effective magnetic field. The effective field has different contributions

$$\mathbf{H}_{\mathrm{eff}}(\mathbf{r},t) = \mathbf{H} + \mathbf{H}_{\mathrm{ex}}(\mathbf{r},t) + \mathbf{H}_{\mathrm{dip}}(\mathbf{r},t), \tag{8}$$

where $\mathbf{H}_{\mathrm{ex}}(\mathbf{r},t)$ is the exchange field and $\mathbf{H}_{\mathrm{dip}}(\mathbf{r},t)$ is the dipolar field. The PWM aims at transforming Eq. (7) into a linearized eigenproblem that can be solved using standard numerical procedures. To obtain the linearized eigenproblem, one relies, first, on the decomposition of the magnetization vector and the demagnetization field into a static and a

dynamic component. For small dynamic components, i.e., small precession amplitudes as present in the experiments, Eq. (7) can be readily linearized.[38] Second, for the magnetic thin film and the magnetization $\mathbf{M}(\mathbf{r},t)$ orientated in the xy plane, the correct boundary conditions are to be considered when solving Maxwell's equation for the dipolar fields. According to the ideas presented in Ref. 39, for a slab of a 2D magnonic crystal with uniform magnetization along its thickness the Maxwell equations can be solved in the magnetostatic approximation with electromagnetic boundary conditions properly taken into account on both surfaces of the 2D magnonic crystal slab. Third, the nonmagnetic portions in the ADL, i.e., the holes, need to be modeled using a strongly reduced but finite saturation magnetization in order to have solutions continuously defined throughout the xy plane. Typically, the reduced saturation magnetization is taken at least 10 times smaller than the M_s of permalloy. It simply serves to obtain convergence in PWM calculations; it is, in particular, not related to the effectively reduced $M_s^\star$ found to describe the dispersion of SWs in the ADL in Sec. III B. Finally, the eigenproblem is solved in momentum space attributing the Bloch theorem to the dynamical components of the magnetization and dipolar field. The magnetic parameters used for the PWM are as follows: film thickness $t_s = 25$ nm, saturation magnetization $M_s = 770$ kA/m, hole diameter $d =$ 140 nm, and out-of-plane anisotropy of 0.7 erg/cm^2.

Furthermore, we have used the software package MICROMAGUS for modeling static and dynamic properties of samples 2 and 3.[40] To model the ADL we have used periodic boundary conditions in the two lateral directions. The following simulation parameters were considered: saturation magnetization $M_s = 780$ kA/m, damping constant $\alpha = 0.005$, exchange constant 1.6×10^{-11} J/m, and out-of-plane anisotropy 0.7 erg/cm^2. The lateral simulation cell size was $p/48 = 800\,\text{nm}/48 \simeq 16.7\,\text{nm}$[41], hole diameter $d =$ 116.9 nm, and film thickness $t_s = 25$ nm. The simulated hole diameter was within the error of the measured average value of hole diameters in the real samples. To obtain the spin-wave dispersions from micromagnetic simulations, 1×85 ADL unit cells in the x and y directions, respectively, were simulated with the two-dimensional periodic boundary conditions. This corresponds to a total simulated area of about $\Delta x \times \Delta y = 0.8 \times 68\ \mu\text{m}^2$. SW propagation was studied along the y direction.[42] The spatiotemporal spin-wave propagation pattern was Fourier transformed to obtain the dispersion $f(k)$.

III. EXPERIMENTAL RESULTS

A. All-electrical spin-wave spectroscopy data

First we discuss the signal amplitudes a_{21} for the three different samples measured between the emitter and detector CPWs at 20 mT. In Fig. 2(a) we vary the angle η and follow the relative change in a_{21}. For each η we show the largest value obtained for a_{21}. The relevant eigenfrequencies will be discussed later. Each sample is found to exhibit a characteristic variation of a_{21} as a function of η. For sample 1, i.e., the plain film, the signal amplitude decreases monotonously with increasing η (dotted line). The maximum is obtained at $\eta = 0°$. For the full ADL (sample 2) the maximum a_{21} is also at $\eta = 0°$ (solid gray line). However, a_{21} decreases

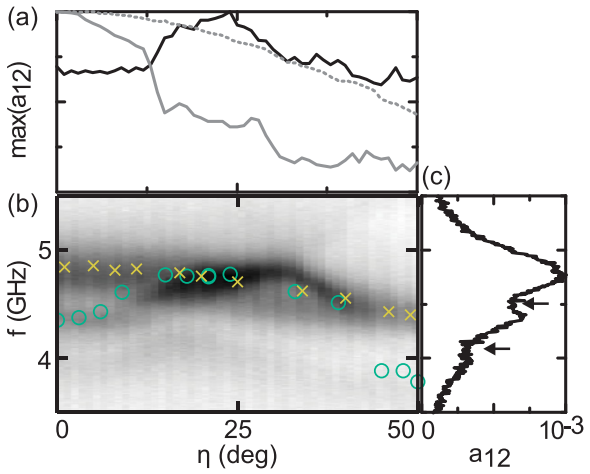

FIG. 2. (Color online) (a) Maximum amplitude max(a_{21}) measured between two CPWs in transmission configuration for sample 1 (plain film, dotted line), sample 2 (full ADL, solid gray line), and sample 3 (hybrid device, black line). We use $\mu_0 H = 20$ mT. (b) Gray-scale plot of spectra $a_{21}(f)$ for different η for sample 3. Dark (bright) represents large (small) SW amplitude. Open circles (crosses) mark the frequency of the main ADL (plain film) mode. (c) $a_{21}(f)$ for $\eta = 0°$, sample 3. Arrows highlight local minima in the resonance curve (see text).

much more pronounced with η than in sample 1. The hybrid device consisting of both plain film and ADL (sample 3) strikingly differs in behavior (solid black line). The signal is not the average of the two former ones. Counterintuitively, the maximum signal is not found at $\eta = 0°$ in the hybrid device. Instead, when SWs are transmitted across the relevant boundary, the maximum amplitude is found at $\eta \approx 25°$. At $\eta = 0°$ and $\eta = 50°$ we find smaller signals being of almost the same strength. This also differs from samples 1 and 2. Sample 3 thus shows unexpected properties that do not reflect the properties of the constituents. In the following, we will attribute this to the transmission characteristics of the boundary itself that has not yet been regarded. We will introduce the field- and frequency-dependent transmission coefficients $t(f)$ of the boundary. For this it is instructive to compare frequency-resolved spectra $a_{21}(f)$ of the three samples. We summarize them in Fig. 2(b). The gray-scale plot shows $a_{21}(f)$ for sample 3. Dark (bright) denotes large (small) amplitude. We find that the characteristic frequency of large SW signal varies with η. The relevant frequencies are between about 4 and 5 GHz. In Fig. 2(c) we show a spectrum $a_{21}(f)$ of the hybrid device at $\eta = 0°$ as a line scan. Overall, we observe a relatively broad resonance with two characteristic minima indicated by arrows. These will be explained later. The main resonances of sample 1 (plain film) and sample 2 (full ADL) are shown as symbols in Fig. 2(b), i.e., crosses and circles, respectively. From this we find that all three samples show SW resonances between about 4 and 5 GHz at 20 mT. For some angles η resonances are found to be degenerate. The resonance frequency of the plain film (sample 1) varies monotonously from about 4.9 to 4.4 GHz with increasing η. This behavior is expected. It originates from the transition of a magnetostatic surface wave (MSSW), where $\mathbf{k} \perp \mathbf{H}$ (at $\eta = 0°$), to a backward volume magnetostatic wave

(BVMSW), where $\mathbf{k} \parallel \mathbf{H}$ (at $\eta = 90°$). At the same time the group velocity v_g decreases with η.[43] Assuming a constant relaxation time for the plain film[32] the signal a_{21} is expected to decrease with increasing η according to Eq. (1). We find this behavior in Fig. 2(a) (dotted line). For the full ADL sample the variation of resonance frequencies with η is found to be much larger and more complex in Fig. 2(b) (circles). Comparing the results with data from the literature it becomes clear that the resonance frequencies between 4 and 5 GHz of the full ADL belong to the so-called extended or fundamental mode.[27,32] This mode has been studied so far mainly for $k = 0$ using micromagnetic simulations and relatively large wave vectors k, i.e., short SW wavelengths, using both inelastic light scattering and AESWS with nanopatterned CPWs.[32] The LWL was not considered in detail. It was shown that for $\eta = 0°$ and large k in the y direction, i.e., perpendicular to $\mathbf{H}$ (cf. Fig. 1), the mode could be described by assuming SWs exhibiting a quantized wave vector $k_\parallel$ between rows of neighboring holes. The wave vector parallel to the field was then given by

$$k_\parallel = n\pi/w_{\text{eff}}, \tag{9}$$

where the effective quantization width w_{eff} was 600 nm for $p = 800$ nm and $\eta = 0$. $n = 1,2,3,\ldots$, is the mode number. The SW dispersion measured for relatively large k perpendicular to the quantization direction, i.e., perpendicular to $\mathbf{H}$ was found to be consistent with the SW dispersion calculated for an individual ferromagnetic nanowire of width $w_{\text{eff}} = 600$ nm assuming $n = 1$.[32] Following this analysis at large $k_\perp$ the ADL seemed to consist of numerous nanowires in parallel. Interaction or coherent coupling from nanowire to nanowire did not seem to be relevant. The dispersion for $n = 1$ taken from Ref. 32 is reproduced in Fig. 3(a) as a dash-dotted line. Strikingly it shows $v_g = 0$ at $f = 4$ GHz for $k \to 0$.

If we now compare the frequency-resolved signal a_{21} of the hybrid device [gray-scale code in Fig. 2(b)] with the eigenfrequencies of both the plain film (crosses) and full ADL (circles) the frequency of maximum a_{21} (black) does not simply follow either the film or ADL resonance frequency. SWs propagating from the film into the ADL in sample 3 behave differently from that. To understand the SW properties of the hybrid device it is now important to explore experimentally the relevant SW dispersion of the ADL in the LWL and compare it to the previously introduced nanowire model highlighted by the dash-dotted line in Fig. 3(a).

B. Spin-wave dispersions of plain film and antidot lattice in the long-wavelength regime

In this section we analyze the SW dispersions in the constituents of sample 3 separately, i.e., in the plain film (sample 1) and the full ADL (sample 2). To measure the SW dispersion, we employ the frequency-resolved MOKE introduced above.[35] We phase-sensitively detect the SWs excited by the sinusoidal driving field h_{rf} at frequency f that propagates away from the emitter CPW. We measure the MOKE signal at two different phases set between the laser probe and the microwave excitation h_{rf}. These two phases are chosen such that they differ by 90° to extract the real and imaginary part of the magnetic susceptibility. We take the MOKE data for a given f as a function of distance from the CPW. By this means

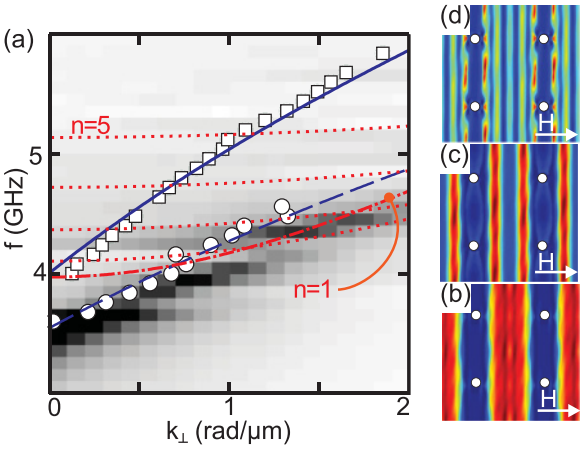

FIG. 3. (Color online) (a) Measured and calculated SW dispersions for a plain film and an ADL at $\mu_0 H = 20$ mT and $\eta = 0$. Open squares mark the MOKE data obtained on a plain film. The solid line reflects the calculated dispersion assuming $M_s = 770$ kA/m.[43] Open circles mark the MOKE data measured on the ADL. The long-dashed line is a SW dispersion calculated for a film assuming a reduced saturation magnetization $M_s^\star = 600$ kA/m. This remodels the measured dispersion far better than previously discussed nanowire SW dispersions[32,44] (see text): the dotted and dashed-dotted lines represent calculated dispersions obtained from a model assuming $M_s = 770$ kA/m and quantized wave vectors $k_\parallel = n\pi/w_{\text{eff}}$ [Eq. (9)] with $w_{\text{eff}} = 600$ nm. The gray-scale plot is the SW dispersion as obtained from wave-vector-resolved micromagnetic simulations (see text). Dark (bright) corresponds to large (small) SW amplitude. Spatial spin-wave profiles as obtained from micromagnetic simulations at $k = 0$ are shown for (b) $f = 3.7$ GHz ($n = 1$), (c) $f = 4.2$ GHz ($n = 2$), and (d) $f = 4.4$ GHz ($n = 3$). Dark (bright) colors correspond to small (large) spin-precession amplitude. The direction of $\mathbf{H}$ is indicated.

we follow the SW's phase change and wavelength λ along the propagation path away from the CPW. We repeat such spatially resolved and microwave-synchronized MOKE experiments for different f and, thereby, evaluate the dispersion relation $f(k)$, where $k = 2\pi/\lambda$ is the measured wave vector of the microwave-excited SW. Figure 3(a) shows the data obtained on a plain 25-nm-thick permalloy film similar to sample 1. The squares mark the SW dispersion measured by the MOKE technique. Using the approach of Ref. 43 we obtain the continuous line as the predicted dispersion $f(k)$ for a thin film exhibiting $M_s = 770$ kA/m. This value is in good agreement with $M_s = 800$ kA/m determined via VNA ferromagnetic resonance.[45,46]

We now discuss the SW dispersion of the ADL (sample 2). Circles in Fig. 3(a) indicate MOKE data obtained for the fundamental mode of the ADL. Following the circles from large k to smaller k we find that the slope, i.e., the group velocity, stays more or less constant. Surprisingly the resonance frequency does not level off and does not exhibit $v_g = 0$ near $k = 0$ as one would have expected from the nanowire model.[32,44] To underline this, we have plotted SW dispersions of the corresponding nanowire as dotted and dash-dotted lines in Fig. 3(a) for different n. All the dispersions deviate from the measured one in the LWL. Figures 3(b), 3(c), and 3(d) illustrate the spin-precession profiles of the modes with $n = 1$, 2, and

3, respectively. These profiles are taken from micromagnetic simulations performed at $k = 0$. Later they will be compared to results based on the PWM which allows us to consider in particular $k \neq 0$.

The wave-vector-resolved ADL data of Fig. 3(a) (circles) which address the LWL in detail give $v_g > 0$ for $k_\perp \to 0$. This behavior is similar to a plain film. In the context of the nanowire model this behavior implies that the quantized wave vector $k_\parallel$ of Eq. (9) is not relevant. Empirically, we find that the data (circles) is described very well by a SW dispersion where we assume a plain film with an effectively reduced magnetization $M_s^\star = 600\,\mathrm{kA/m}$ (dashed line). In the context of metamaterials one interpretation of this finding is that the dynamic response of the ADL is effectively continuous, i.e., the ADL acts for SWs as if a plain film of effective magnetic parameters was present. This consideration will be further explored when discussing the separate experiment on SW transmission across the boundary of sample 3 in the next section.

C. Frequency dependence of spin-wave transmission from the plain film into the ADL

Using the spatially resolved MOKE experiment combined with microwave excitation at frequency f we have measured SW amplitudes locally at different distances away from the SW emitter along the y direction. The signal is depicted as the solid dark line in Fig. 4(a). Equation (6) is fitted to the MOKE data [dashed line in Fig. 4(a)]. We find $\xi_{\mathrm{film}} = 0.1\ \mu\mathrm{m}^{-1}$ in good agreement with previously published data.[32] From the fitted MOKE data we recalculate the transmission coefficient t considering the relative strengths of amplitudes at the interface via

$$t = 1 - r = 1 - \frac{a_{0,\mathrm{out}}^{\mathrm{film}}}{a_{\mathrm{in}}^{\mathrm{film}} \exp(-\xi y_0)}. \qquad (10)$$

Values obtained for different f by this method are plotted in Fig. 5(a) as solid circles. The transmission coefficient varies from $t = 0.25$ near 4 GHz to almost 0.8 near 5 GHz. It changes by about a factor of 3 within 1 GHz. The two data points

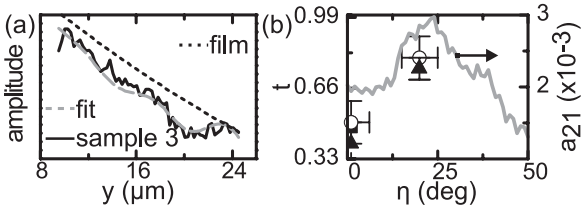

FIG. 4. (a) $\eta = 0°$. SW amplitude between emitter and boundary of the ADL measured by MOKE at $f = 4.48$ GHz (depicted as a continuous line). This shows an interference pattern due to partial back-reflection of SWs at the boundary. The CPW outer conductor edge (boundary) is at $y = 8(25)\ \mu$m. A fitted function according to Eq. (6) considers the incident and back-scattered SWs (long-dashed line). The short-dashed line indicates the nonoscillatory decay that would have been expected for a plain film without a boundary. It is arbitrarily shifted with respect to the other curve for clarity. (b) $t(\eta)$ from AESWS (open circles), MOKE measurements (solid square at $\eta = 0°$), and micromagnetic simulations (solid triangles). The solid line depicts the maximum transmission amplitude max(a_{21}) as obtained via AESWS [from Fig. 2(a)].

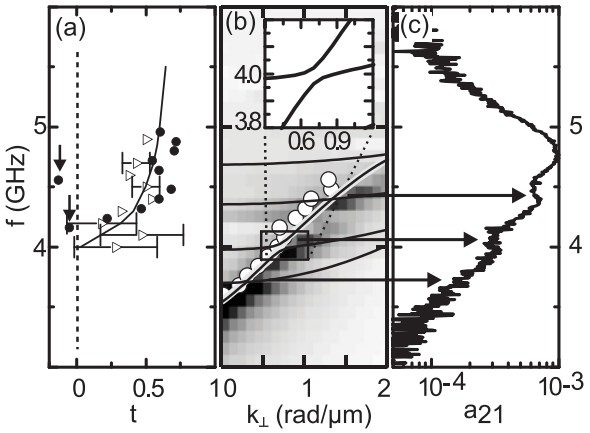

FIG. 5. (a) Transmission coefficient t for SWs propagating from the plain film into the ADL of sample 3. Solid circles represent data obtained by MOKE. The continuous function (solid line) follows from the dispersions fitted to the measured data of samples 1 and 2 in Fig. 2(a). It is calculated using Eq. (2) and represents an independent consistency check of the data measured on sample 3. The data with $t < 0$ at $f = 4.05$ and 4.5 GHz are marked with arrows and explained in the text. Triangles depict simulated results obtained from the wave-vector-resolved micromagnetic simulations. (b) Solid lines represent SW dispersions of the ADL as obtained by the PWM. To aid the comparison the gray-scale plot and MOKE data (circles) of Fig. 3(a) are reproduced. The inset is a magnification of one of the three anticrossings observed in the PWM data. (c) Spectrum $a_{21}(f)$ measured by AESWS for $\eta = 0°$ [replotted from Fig. 2(c)]. We attribute local minima in $a_{21}(f)$ with avoided crossings predicted by the PWM (highlighted by arrows).

evaluated at $f = 4.05$ and $f = 4.55$ GHz with $t < 0$ (marked by arrows) deviate strongly from the other values and will be discussed separately. $t < 0$ is a consequence of the evaluation method and corresponds to very low transmission values.

Let us now compare the measured data of sample 3 with calculated transmission coefficients. Following Eq. (2) we assume at a given f that a SW of wave vector $k_1(f)$ originates from medium 1 and propagates into medium 2 with $k_2(f)$. Based on the experimental data of Fig. 3(a) obtained on samples 1 and 2 we consider for medium 1 (2) the thin-film SW dispersions calculated for $M_s = 770\,\mathrm{kA/m}$ ($M_s^\star = 600\,\mathrm{kA/m}$). These two curves have been found to remodel well the experimental values $f(k_1)$ and $f(k_2)$ for medium 1 and medium 2, respectively. Introducing the relevant values k_1 and k_2 at different f into Eq. (2), one ends up with the continuous function $t(f)$ displayed as a solid line in Fig. 5(a). This is the transmission coefficient expected from SW measurements performed separately on the individual constituents of sample 3. The data measured directly on sample 3 (solid circles) are consistent with the calculated trace. The large variation of t in a frequency range of about 1 GHz is remodeled well. As a result the transmission (and reflection) coefficient for the SWs measured by MOKE can be described as if two continuous media were present forming the boundary. In the framework of a metamaterial and long wavelength SWs the magnetic ADL of large permalloy filling fraction $\mathcal{F}$ is surprisingly well described by assuming an artificial material with an effectively continuous property, i.e., the effectively

reduced magnetization $M_s^\star$. Note that $M_s^\star$ deviates from the arithmetic average $\mathcal{F} \times M_s = 757$ kA/m. It is found to be significantly smaller. The tiny holes alter the dynamic response considerably.

The MOKE technique making use of Eq. (6) is reliable for measuring t if a sufficient number of oscillations between the CPW and boundary was resolved. This has not been the case for $\eta > 0$, where the SW signal is found to be too weak due to the reduced group velocity v_g.[43] For $\eta \geqslant 0$, the AESWS technique has turned out to be powerful in exploring SW propagation phenomena.

D. Angular dependence of spin-wave transmission into the ADL

For AESWS, we rely on the signal amplitudes measured at fixed CPW positions before and behind the boundary; this differs from the MOKE technique where we scanned the laser probe beam. The spin-wave excitation (detection) strength is given by a_0, i.e., the signal amplitude measured in reflection configuration. a_{21} denotes the signal amplitude in transmission configuration. Following Eq. (1) we write for the plain film (sample 1)

$$a_{21}^{\text{film}} / a_0^{\text{film}} = \exp(-s \times \xi_{\text{film}}). \tag{11}$$

For the antidot lattice (sample 2) we consider $\xi_{\text{lattice}} = \text{Im}k_2$ accordingly. We use Eq. (11) and measurements on samples 1 and 2 to determine ξ_{film} and ξ_{lattice}, respectively. These values are needed as a reference as discussed below. For $\eta = 0^\circ$, we find $\xi_{\text{film}} = 0.12 \pm 0.02\ \mu\text{m}^{-1}$ in good agreement with MOKE data, and $\xi_{\text{lattice}} = 0.15 \pm 0.02\ \mu\text{m}^{-1}$. Sample 3 is not symmetric; here $a_{22} \neq a_{11}$. The amplitude in sample 3 is

$$a_{21}/a_{11} = t \exp[-(s - \chi)\xi_{\text{film}}] \exp(-\chi \xi_{\text{lattice}}). \tag{12}$$

By evaluating Eqs. (11) and (12) to obtain t, we take into account the different SW decay lengths ξ in the antidot lattice and the plain film. In this approach, measurements on three separate samples enter, and one has to be careful that the signal levels in all samples are sufficiently large. In our samples this is the case for the frequencies corresponding to maximum amplitude in the ADL [circles in Fig. 2(b)]. As a consequence, we do not obtain a fully frequency-resolved transmission coefficient $t(f)$ as calculated from Eq. (2). For $\eta = 0^\circ$ and $f = 4.4$ GHz, we find a value of $t = 0.5 \pm 0.1$ in good agreement with MOKE results shown in Fig. 5(a). Using AESWS, we have obtained t at $\eta = 20^\circ \pm 5^\circ$ as well. Because of the smaller signal-to-noise ratio, this value is taken as an average over the angular regime going from 15° to 25°. We get $t(\eta = 20^\circ \pm 5^\circ) = 0.8 \pm 0.1$. This value is significantly larger than $t = 0.5 \pm 0.1$ obtained at $\eta = 0^\circ$. To analyze the origin of the large value, knowledge of the dispersions to access Eq. (2) would be helpful. However, for $\eta > 0^\circ$, it was not possible to measure SW dispersions by MOKE due to low v_g.[32] Importantly, the frequencies of the eigenmodes in the antidot lattice and in the plain film are found to be almost degenerate in this angular regime [Fig. 2(b), open circles and crosses, respectively]. Sample 3 exhibits a very large SW amplitude at the same frequency as well. Even without the knowledge of SW dispersions in misaligned fields, we assume $k_1 \approx k_2$ giving rise to a large value of t following Eq. (2).

We summarize the experimental findings at this point: First, the SW dispersion of the fundamental mode within the ADL was found to deviate in the LWL from the previously made observation of a wire mode quantized in the direction of **H**. Instead, it is found to be described rather well by a constant v_g for small k and effectively continuous properties. Second, based on this, the transmission coefficients of SWs entering the ADL from a film is found to be described well by Eq. (2). Third, the transmission coefficient is found to depend on the frequency and angle. In the following, we present theoretical approaches to understand the observations in greater detail.

IV. THEORETICAL RESULTS

We have performed both calculations using the plane-wave method and wave-vector-resolved micromagnetic simulations. The two techniques have different advantages: the PWM allows for a high wave-vector resolution when calculating the dispersion of SWs in an ADL; however, calculation of SWs propagating across a boundary is not possible. Differently, micromagnetic simulations allow for simulation of complex geometries, including the boundary. The wave-vector resolution is, however, limited due to computational restrictions (restricted computational power).

A. Modes and SW dispersions calculated by the plane-wave method

Dispersions of different eigenmodes as obtained from PWM calculations for sample 2 are depicted as solid lines in Fig. 5(b) for $\eta = 0^\circ$. There exists in particular a specific dispersion with a relatively large and almost constant slope (constant v_g) that is crossing with several dispersions having $v_g \approx 0$. The specific dispersion is highlighted by a broad light-gray line. It obeys $v_g > 0$ for $k \to 0$, consistent with our experimental observations in the LWL.

For the parameter sets ($k = 0.3$ rad/μm, $f = 3.7$ GHz) and ($k = 1.3$ rad/μm, $f = 4.4$ GHz) crossings and for ($k = 0.7$ rad/μm, $f = 4.0$ GHz), an avoided crossing is predicted by the PWM (marked by horizontal arrows). Near two of these frequencies ($f = 4.0$ GHz and $f = 4.4$ GHz), the measured spectrum a_{21} exhibits local minima as depicted in Fig. 5(c).[47]

To understand the origin of two types of crossings, it is instructive to study the spatial spin-wave profiles associated with the eigenmodes at different values of the wave vector, i.e., $k = 0$ rad/μm [Figs. 6(a)–6(d)], $k = 0.5$ rad/μm [Figs. 6(e)–6(h)], and $k = 1$ rad/μm [Figs. 6(i)–6(l)]. For $k = 0$, the spatial SW profiles of the first four modes, followed in the order of increasing frequency, correspond to the quantization [Eq. (9)] $\pi n / w_{\text{eff}}$ with $n = 1,2,3,4$. These modes can be divided into two groups: symmetric and antisymmetric modes with respect to the axis between the antidots, $n = 1,3$ and $n = 2,4$ modes, respectively. The profiles obtained by the PWM agree well with micromagnetic simulation data shown in Fig. 3(b)–3(d). Interestingly, for $k = 0.5$ rad/μm, the order of mode quantization from low frequencies to high frequencies is $n = 2,1,3,4$ [Figs. 6(e)–6(h)] and for $k = 1.0$ rad/μm the order is $n = 2,3,1,4$ [Figs. 6(i)–6(l)]. This is because for $k = 0.3$ rad/μm there is a crossing between modes of different symmetry: symmetric with antisymmetric (mode

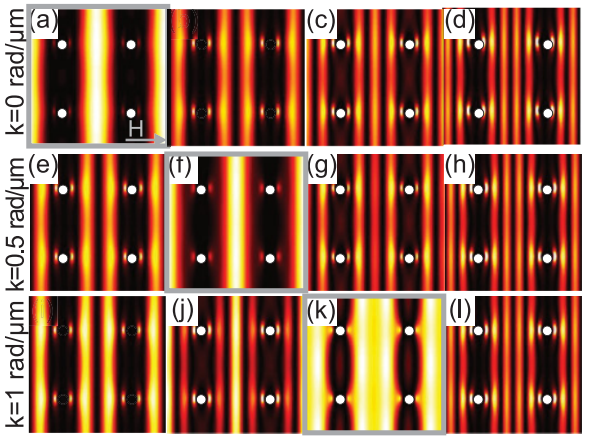

FIG. 6. (Color online) Modulus of spatial SW profiles as calculated by the PWM at $\mu_0 H = 20$ mT and $\eta = 0^\circ$ for $k_\perp$ amounting to (a)–(d) 0 rad/μm, (e)–(h) 0.5 rad/μm, and (i)–(l) 1.0 rad/μm. The number of nodes $(n-1)$ in the direction of **H** is changing. In each row $n = 1$ is highlighted by a thick border. It is found in different columns. This illustrates the avoided crossing predicted in the SW dispersions of the PWM. The specific parameters are as follows: (a) $f = 3.5$ GHz, $n = 1$; (b) 3.7 GHz, $n = 2$; (c) $f = 4.0$ GHz, $n = 3$; (d) $f = 4.4$ GHz, $n = 4$; (e) $f = 3.7$ GHz, $n = 2$; (f) $f = 3.8$ GHz, $n = 1$; (g) $f = 4.0$ GHz, $n = 3$; (h) $f = 4.4$ GHz, $n = 4$; (i) $f = 3.8$ GHz, $n = 2$; (j) $f = 4.0$ GHz, $n = 3$; (k) $f = 4.2$ GHz, $n = 1$; (l) $f = 4.4$ GHz, $n = 4$. Bright color indicates a large spin-precession amplitude.

$n = 1$ with $n = 2$). Hybridization between them does not occur and the profiles preserve their shape. For $k = 0.7$ rad/μm, an avoided crossing is predicted between the modes $n = 1$ and $n = 3$ as shown in the inset in Fig. 5(b). As both modes are symmetric, hybridization occurs and changes in SW profiles can be observed [cf. Fig. 6(f) and 6(k)]. The crossing for $f = 4.4$ GHz is again between the even and odd modes and hybridization is not expected for the perfect ADL. The measured spectrum a_{21} exhibits local minima for both $f = 4.1$ and 4.4 GHz. The minimum of a_{12} at $f = 4.1$ GHz is attributed to the avoided crossing between the symmetric modes. From this a forbidden frequency gap results and the ADL does not support SWs. The situation is more complex at $f = 4.4$ GHz where also a minimum of a_{12} is observed. We believe that both damping and unintentional breaking of the mirror symmetry due to variations in the hole shapes lifts orthogonality between the antisymmetric and symmetric modes. This results in an avoided crossing between the participating modes. Considering this, one expects that the splitting of the SW spectrum into the even and odd modes is canceled and the hybridization can exist even between the modes of different symmetry. This has not been remodeled by the PWM assuming a perfect ADL, i.e., PWM predicts a crossing instead of the avoided crossing. Still, the relevant frequency is consistent with the experiment.

B. Micromagnetic simulations of transmission into the ADL

We now model the propagation of SWs across the boundary between a plain film and an ADL. This is not possible with the PWM but the micromagnetic simulations. First, we address the simulated SW dispersion of the ADL alone. This dispersion is depicted as a gray-scale plot in Fig. 3(a) and is replotted in Fig. 5(b). The simulated dispersion agrees well with the MOKE experiments [Fig. 3(a)] and calculations performed by the PWM [Fig. 5(b)]. In particular, one finds $v_g > 0$ for the fundamental mode at $k \to 0$.

Micromagnetic simulations now allow us to model the spin-wave transmission into the ADL. For this, only a part of the simulation geometry is designed to contain the ADL. The field pulse is centered around $y_{ex} = 27$ μm (emitter region). The plain film is located at $y \leqslant y_0 = 33$ μm, and the ADL lattice is at $y > 33$ μm. The simulated spatiotemporal spin precession is depicted in Fig. 7(a). The SW packets propagating away from the emitter are clearly resolved. At the boundary between the film and the ADL, partial reflection occurs. Within the ADL, the group velocity v_g is found to be reduced. This has been observed recently.[32] In Fig. 7(b) the maximum spin precession amplitude (taken over all simulation times) is plotted for $0 \leqslant y \leqslant 45$ μm.[48] One finds that for $y < 27$ μm the signal amplitude decreases exponentially away from the emitter. This is due to SW damping with increasing time and propagation distance following Eq. (1). The same decay is found for $27\mu\text{m} \leqslant y \lesssim 32$ μm, i.e., toward the film-ADL boundary. The continuous thick lines in Fig. 4 mark exponential fits to this decay: $a_{\text{film}}(y) = a_0 \exp[-(y - y_{ex})\xi_{\text{film}}]$. We find $\xi_{\text{film}} = 0.10\,\mu\text{m}^{-1}$. For $y \gtrsim 34$ μm the same fit (dashed line) yields $\xi_{\text{lattice}} = 0.17\,\mu\text{m}^{-1}$. At the boundary

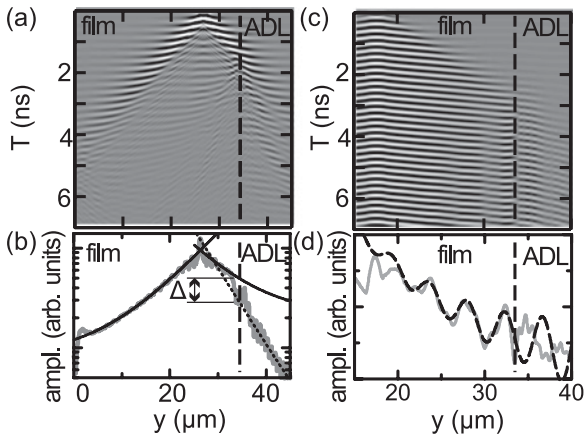

FIG. 7. (a) Spatiotemporal spin-wave precession for pulsed excitation in the plain film at time $T = 0.1$ ns and $y_{ex} = 27$ μm. The film-ADL boundary is located at $y_0 = 33$ μm and marked by the vertical dashed line. Dark (light) colors denote large positive (negative) precession. (b) Maximum SW amplitude over all simulation times (light gray). Exponential fits to the data are depicted as dark solid and dotted lines. At the boundary between the ADL and the film, a sudden decrease in the maximum amplitude Δ due to partial reflection is observed. From this the transmission coefficient t is evaluated (see text). (c) Spatiotemporal spin-wave precession for continuous-wave microwave excitation in the plain film where $y_{ex} = 17$ μm and $f = 4.7$ GHz. For $T \gtrsim 5$ ns, a steady state is reached and minima and maxima of the amplitude are observed in between the excitation region and the boundary (positioned at $y_0 = 33$ μm). (d) Maximum SW amplitude for $T > 5$ ns (gray solid line). The sinusoidal interference pattern is visible. The black dashed line is a fit to the data corresponding to Eq. (6) from which t is evaluated.

$y = y_0 = 33\ \mu$m, locally the maximum spin precession amplitude deviates from the exponential decay. This is due to interface effects and partial reflection. Here we evaluate the signal amplitudes of the fitted decay curves to obtain the transmission coefficient

$$t = 1 - r = 1 - a_{\text{lattice}}(y = y_0)/a_{\text{film}}(y = y_0). \quad (13)$$

Using Eq. (13), we find for $\eta = 0^\circ$ $t = 0.7 \pm 0.1$, in very good agreement with the data obtained by MOKE for $f >$ 4.5 GHz. While these time-resolved simulations are intuitive and illustrate the physics well, frequency-resolved simulations allow for a higher accuracy when determining t.

To obtain frequency-resolved values for t, it is necessary to excite spin waves with a sinusoidal driving field and to use Eq. (6) to fit the relevant interference pattern. The same simulation geometry as described above is used for such a cw excitation; only the emitter region is centered around $y_{\text{ex}} =$ 17 μm in order to have a greater distance between emitter and boundary ($y_0 = 33\ \mu$m). This allows us to better resolve the interference effect. Results obtained for $f = 4.7$ GHz are depicted in Figs. 7(c) and 7(d). Figure 7(c) shows the spatio-temporal spin precession. For times $T > 5$ ns a steady state is reached: for $20 \leqslant y \leqslant 30\ \mu$m, a SW interference pattern with minima and maxima of the precession is resolved in the film. This interference pattern in the SW amplitude is depicted in Fig. 7(d) as the gray continuous line; it is obtained by taking the maximum values of the simulated precession where only $T >$ 5 ns is taken into account, i.e., in the steady state. The fit using Eq. (6) is depicted as a black dashed line. For this analysis, the position of the excitation y_{ex} and the boundary y_0 have been adapted in Eq. (6) to fit the simulated geometry. From this analysis, a transmission coefficient $t = 0.52$ is evaluated at $f = 4.7$ GHz. This data point is depicted along with t obtained for various frequencies f in Fig. 5(a) as open triangles. Such simulated values of t resemble the measured and calculated dependency t vs. f in both quantitative as well as qualitative behavior very well. This simulation may, therefore, serve as an independent verification of Eq. (2) describing well the SW transmission from a film into the nanostructured ADL.

Importantly, the micromagnetic simulations allow us to consider field orientations with $\eta \neq 0$ for sample 3. For $\eta = 20^\circ$ we obtain a value of $t = 0.75 \pm 0.05$. This is in good agreement with the AESWS measurements presented in Sec. III D. The values for t obtained from frequency resolved micromagnetic simulations are depicted in Fig. 4(b) as solid triangles. They agree well with experimental data obtained through AESWS.

V. DISCUSSION

Combining different experimental techniques and theoretical models we have explored the transmission coefficient t of SWs across a boundary between a thin film and an ADL. This is a relevant configuration for future applications in magnonics where the transmission and manipulation of spin waves with magnonic crystals is considered. In contrast to earlier studies, our data obtained in the LWL do not reflect the nanowire model of spin-wave propagation in ADLs. Instead, the SW dispersion and the transmission across the boundary can be understood in terms of an ADL being an effectively continuous material with a reduced magnetization $M_s^\star$. All experimental techniques and theoretical approaches are consistent concerning this outcome. Microscopically we attribute this behavior to dipolar coupling between the SWs residing in stripelike regions of large spin-precession amplitude inside the ADL [cf. Figs. 3(b) to 3(d) and 6]. We expect the SWs separated by a row of holes to oscillate in a coherent manner. Thus, the originally discussed transversal quantization seems to be less effective and does not seem to govern the SW dispersion of the ADL in the LWL. Still, SW profiles are affected by the periodic internal field modulation introduced by the holes as illustrated by the PWM and micromagnetic simulations. Intriguingly, the effectively continuous material properties discussed here seem to originate from the complex interplay of different modes in the ADL.

The PWM dispersions in Fig. 5(b) are found to be partly consistent with the wire model calculations depicted in Fig. 3(a). Away from $k = 0$ the same types of modes are predicted. However, in great contrast to the wire model, the PWM reproduces the finite group velocity v_g in the LWL for the fundamental mode with $n = 1$. This is in good agreement with the experimental observation. In addition, avoided crossings between $n = 1$ and higher-order modes are predicted. At an avoided crossing, a forbidden frequency gap is known to open. In this case, transmission through the ADL is no longer possible and a_{21} should be reduced as substantiated experimentally by the observed local minima. At the same frequencies the analysis of the MOKE data has provided $t < 0$ in Fig. 5(a). This suggests independently that transmission is not possible. Note that the MOKE measurements on reflectivity r (and thus transmission coefficient t) are performed on the plain film part of sample 3. The (unknown) propagation properties inside the ADL are, therefore, not affecting the measurements of SW reflectivity via MOKE.[49] The increased reflectivity of the ADL might be interesting for a frequency-selective spin-wave mirror. Interestingly, such a mirror is fabricated from one and the same ferromagnetic thin film. By using focused ion beam etching it can be integrated in a straightforward manner at different positions in a magnonic device. The orientation of the relevant boundary can be optimized with respect to the incident SW.

VI. CONCLUSIONS

In conclusion, we have studied SWs propagating within and transmitted into a periodic array of holes, i.e., an ADL, characterized by small holes compared to its unit cell size. Only 1.7% of the magnetic material is removed by introducing the hole lattice in a thin $Ni_{80}Fe_{20}$ film. In the limit of SWs with a wavelength much larger than the periodicity $p = 800$ nm, it was found by means of frequency resolved MOKE that the dispersion was not dominated by quantization effects; it was rather well described by a plain film dispersion considering an effectively reduced saturation magnetization $M_s^\star$. The measured dispersion was verified by means of micromagnetic simulations and the plane-wave method. The effectively continuous material dispersion was also found to describe well SW transmission from a plain film into the

ADL. A distinct frequency dependence was resolved. The transmission coefficient was found to vary between 0.25 and 0.8. This was verified by means of frequency resolved micromagnetic simulations. The transmission coefficient was varied by the orientation of the external field. For an angle η of about 25° between the field and ADL boundary, we observed the largest transmission coefficient of $t = 0.8$. For $\eta = 0°$ we found a large reflectivity of the ADL boundary at a few selected frequencies. We attributed this to avoided crossings of ADL modes and the opening of forbidden frequency gaps. In the framework of metamaterials the findings suggested the ADL to exhibit effectively continuous properties for spin waves in the long-wavelength limit.

ACKNOWLEDGMENTS

Financial support by the German Excellence Cluster Nanosystems Initiative Munich (NIM) and the European Community's Seventh Framework Programme (FP7/2007-2013) under Grant No. 228673 MAGNONICS is gratefully acknowledged. The authors thank D. V. Berkov for support using MicroMagus.

*grundler@ph.tum.de

[1] R. A. Shelby, D. R. Smith, and S. Schultz, Science **292**, 77 (2001).
[2] N. Raj and D. R. Tilley, Phys. Rev. B **36**, 7003 (1987).
[3] N. S. Almeida and D. L. Mills, Phys. Rev. B **38**, 6698 (1988).
[4] F. C. Nörtemann, R. L. Stamps, R. E. Camley, B. Hillebrands, and G. Güntherodt, Phys. Rev. B **47**, 3225 (1993).
[5] R. L. Stamps, R. E. Camley, F. C. Nörtemann, and D. R. Tilley, Phys. Rev. B **48**, 15740 (1993).
[6] R. V. Mikhaylovskiy, E. Hendry, and V. V. Kruglyak, Phys. Rev. B **82**, 195446 (2010).
[7] V. V. Kruglyak, R. J. Hicken, A. N. Kuchko, and V. Y. Gorobets, J. Appl. Phys. **98**, 014304 (2005).
[8] N. I. Polushkin, S. A. Michalski, L. Yue, and R. D. Kirby, Phys. Rev. Lett. **97**, 256401 (2006).
[9] V. V. Kruglyak, P. S. Keatley, A. Neudert, R. J. Hicken, J. R. Childress, and J. A. Katine, Phys. Rev. Lett. **104**, 027201 (2010).
[10] C. R. Simovski, Opt. Spectrosc. **107**, 726 (2009).
[11] C. Simovski and S. Tretyakov, Photonic. Nanostruc. **8**, 254 (2010).
[12] C. R. Simovski, J. Opt. **13**, 013001 (2011).
[13] J. B. Pendry, Phys. Rev. Lett. **85**, 3966 (2000).
[14] J. B. Pendry, D. Schurig, and D. R. Smith, Science **312**, 1780 (2006).
[15] D. Schurig, J. J. Mock, B. J. Justice, S. A. Cummer, J. B. Pendry, A. F. Starr, and D. R. Smith, Science **314**, 977 (2006).
[16] R. E. Camley, T. J. Parker, and S. R. P. Smith, Phys. Rev. B **53**, 5481 (1996).
[17] M. P. Kostylev, A. A. Serga, T. Schneider, T. Neumann, B. Leven, B. Hillebrands, and R. L. Stamps, Phys. Rev. B **76**, 184419 (2007).
[18] T. Neumann, A. A. Serga, B. Hillebrands, and M. P. Kostylev, Appl. Phys. Lett. **94**, 042503 (2009).
[19] A. V. Vashkovskii and E. H. Lokk, Phys. Usp. **47**, 601 (2004).
[20] H. Xi, X. Wang, Y. Zheng, and P. J. Ryan, J. Appl. Phys. **104**, 063921 (2008).
[21] S.-K. Kim, S. Choi, K.-S. Lee, D.-S. Han, D.-E. Jung, and Y.-S. Choi, Appl. Phys. Lett. **92**, 212501 (2008).
[22] D.-E. Jeong, D.-S. Han, S. Choi, and S.-K. Kim, Spin **1**, 27 (2011).
[23] M. Dvornik, A. N. Kuchko, and V. V. Kruglyak, J. Appl. Phys. **109**, 07D350 (2011).
[24] S. Neusser and D. Grundler, Adv. Mater. **21**, 2927 (2009).
[25] V. V. Kruglyak, S. O. Demokritov, and D. Grundler, J. Phys. D: Appl. Phys. **43**, 264001 (2010).
[26] M. J. Pechan, C. Yu, R. L. Compton, J. P. Park, and P. A. Crowell, J. Appl. Phys. **97**, 10J903 (2005).
[27] S. Neusser, B. Botters, and D. Grundler, Phys. Rev. B **78**, 054406 (2008).
[28] B. K. Kuanr, L. M. Malkinski, M. Yu, D. Scherer, R. Camley, and Z. Celinski, *Technical Proceedings of the 2008 NSTI Nanotechnology Conference and Trade Show, Boston*, edited by M. Laudon and B. Romanowicz (CRC Press, Boca Raton, 2008), Vol. 1, pp. 542–545.
[29] H. Ulrichs, B. Lenk, and M. Münzenberg, Appl. Phys. Lett. **97**, 092506 (2010).
[30] F. Giesen, J. Podbielski, T. Korn, M. Steiner, A. van Staa, and D. Grundler, Appl. Phys. Lett. **86**, 112510 (2005).
[31] M. Bailleul, D. Olligs, and C. Fermon, Phys. Rev. Lett. **91**, 137204 (2003).
[32] S. Neusser, G. Durr, H. G. Bauer, S. Tacchi, M. Madami, G. Woltersdorf, G. Gubbiotti, C. H. Back, and D. Grundler, Phys. Rev. Lett. **105**, 067208 (2010).
[33] M. L. Schneider, J. M. Shaw, A. B. Kos, T. Gerrits, T. J. Silva, and R. D. McMichael, J. Appl. Phys. **102**, 103909 (2007).
[34] G. Woltersdorf and C. H. Back, Phys. Rev. Lett. **99**, 227207 (2007).
[35] I. Neudecker, F. Hoffmann, G. Woltersdorf, and C. H. Back, J. Phys. D: Appl. Phys. **41**, 164010 (2008).
[36] J. Podbielski, D. Heitmann, and D. Grundler, Phys. Rev. Lett. **99**, 207202 (2007).
[37] F. Schwabl, *Quantenmechanik* (Springer, Berlin, 2002).
[38] M. Krawczyk and H. Puszkarski, Phys. Rev. B **77**, 054437 (2008).
[39] J. Kaczer and L. Murtinova, Phys. Status Solidi A **23**, 79 (1974).
[40] D. V. Berkov and N. L. Gorn, MICROMAGUS: *Software for Micromagnetic Simulations* (2008), [http://www.micromagus.de].
[41] To simulate the SW propagation from the plain film into the ADL we needed to consider a propagation length of 68 μm at a width of 0.8 μm. At the same time the device needed to be subdivided in a mesh of nanoscopic simulation cells giving rise to a large total number of cells. Taking a lateral cell size of 16.7 nm we obtained about 2×10^5 simulation cells to be handled numerically in the time-resolved micromagnetic simulation. This number was still a challenge. Smaller cell sizes provoked data overflow. The lateral discretization size of 16.7 nm allowed us to simulate the long-wavelength SW excitations of the film and ADL. We note that thereby we underestimated exchange effects as the exchange length was about 5 nm. However, the relevant dipolar interactions relevant at the long wavelengths considered here were covered.

[42] A short field pulse excited SWs with frequencies up to ≈50 GHz; the field pulse had a spatial extent of 2 μm in the y direction (no dependence on x coordinate) and the amplitude was 0.2 mT. We have tested the robustness of results by varying M_s between 760 and 860 kA/m, and set the film thickness to $t_s = 22$ nm and $t_s = 28$ nm. No significant changes in the obtained results, i.e., in the transmission coefficients t and mode profiles were observed and we included the ≈5% variation in the error bars of Fig. (4b).

[43] B. Kalinikos and A. Slavin, J. Phys. C: Solid State Phys. **19**, 7013 (1986).

[44] V. E. Demidov, J. Jersch, S. O. Demokritov, K. Rott, P. Krzysteczko, and G. Reiss, Phys. Rev. B **79**, 054417 (2009).

[45] F. Giesen, J. Podbielski, T. Korn, and D. Grundler, J. Appl. Phys. **97**, 10A712 (2005).

[46] S. S. Kalarickal, P. Krivosik, M. Wu, C. E. Patton, M. L. Schneider, P. Kabos, T. J. Silva, and J. P. Nibarger, J. Appl. Phys. **99**, 093909 (2006).

[47] For $f = 3.7$ GHz, the local minimum of a_{21} is not resolved. Here, the signal amplitude is very weak because the mode is below the ferromagnetic resonance frequency in the plain film of $f = 4.0$ GHz. Most probably, the signal-to-noise ratio is too small to observe the feature.

[48] By taking the maximum amplitude, only the primary SW packet is taken into account and, in particular, not the reflected SW packet as it has a smaller amplitude.

[49] We note that increased damping is observed using AESWS within the ADL. The AESWS technique is, therefore, not suited to obtain t because it relies on a high signal-to-noise ratio and exact knowledge of ξ_{lattice}.